

Multidomain Memristive Switching of Pt₃₈Mn₆₂/[Co/Ni]_n Multilayers

G. K. Krishnaswamy,^{1,*} A. Kurenkov^{2,3,4,†} G. Sala,¹ M. Baumgartner,¹ V. Krizakova^{2,§} C. Nistor,¹ F. Maccherozzi,⁵ S. S. Dhesi,⁵ S. Fukami^{2,3,4,6,7,‡} H. Ohno,^{2,3,4,6,7} and P. Gambardella^{1,§}

¹ Department of Materials, ETH Zurich, Switzerland

² Center for Science and Innovation in Spintronics, Tohoku University, Sendai 980-8577, Japan

³ Center for Spintronics Research Network, Tohoku University, Sendai 980-8577, Japan

⁴ Laboratory for Nanoelectronics and Spintronics, Research Institute of Electrical Communication, Tohoku University, Sendai 980-8577, Japan

⁵ Diamond Light Source, Chilton, Didcot, Oxfordshire OX11 0DE, United Kingdom

⁶ Center for Innovative Integrated Electronics Systems, Tohoku University, Sendai 980-0845, Japan

⁷ WPI Advanced Institute for Materials Research, Tohoku University, Sendai 980-8577, Japan



(Received 4 July 2020; accepted 22 September 2020; published 20 October 2020)

We investigate the mechanism of analoglike switching of Pt₃₈Mn₆₂/[Co/Ni] multilayers induced by spin-orbit torques. X-ray photoemission microscopy performed during magnetization reversal driven by current pulses shows that sequential switching of reproducible domain patterns can be achieved. Switching proceeds by domain-wall displacement starting from the edges of blocked ferromagnetic domains, which do not switch for either direction of the current and represent up to 24% of the total ferromagnetic area. The antiferromagnetic Pt₃₈Mn₆₂ layer has a granular texture, with the majority of the domains being smaller than 100 nm, whereas the ferromagnetic domains in Co/Ni are typically larger than 200 nm. The blocked domains and the granular distribution of exchange bias constrain the origin as well as the displacement of the domain walls, thus leading to highly reproducible switching patterns as a function of the applied current pulses. These measurements clarify the origin of the memristive behavior in antiferromagnet-ferromagnet structures and provide clues for further optimization of spin-orbit torque switching and memristivity in these systems.

DOI: 10.1103/PhysRevApplied.14.044036

I. INTRODUCTION

Current-induced magnetization reversal of ferromagnetic materials using spin-orbit torques (SOTs) [1] has been successfully demonstrated in different implementations of heavy metal–ferromagnet bilayers [1–10]. In these systems, the SOTs are mediated by the transverse spin accumulation created at the interface between the heavy metal and the ferromagnet by the spin Hall effect and interfacial spin scattering [1,2,11–15]. At current densities exceeding approximately 10¹¹ A/m², the SOTs induce the nucleation of reversed domains and propagation of the domain wall, which eventually lead to switching of the ferromagnet [16–20]. The high switching speed, low error rate, and reproducible reversal behavior make SOTs very attractive to control the magnetization of perpendicular storage media [21–27]. However, the

switching of a magnetic layer with perpendicular magnetization usually requires the breaking of symmetry by a static field collinear with the current, as the SOTs alone do not discriminate between the up and down states of a ferromagnet [2].

In previous studies, symmetry breaking in the absence of an external field has been achieved by permanent magnets integrated in the switching device [2,28], asymmetric patterning [29–31], and exchange coupling to a ferromagnetic [32] or antiferromagnetic layer [33–36]. The employment of an antiferromagnet creates an exchange bias at the interface with the ferromagnet that acts as a symmetry-breaking field [Figs. 1(a) and 1(b)]. Whereas a heavy metal can be additionally introduced to such a system to obtain interfacial spin accumulation [34], some metallic antiferromagnets such as platinum manganese present strong spin-orbit coupling and can perform the role of the heavy metal [33,35–39], thus allowing dual functionality. The stacking of ferromagnets and antiferromagnets also permits the fabrication of a magnetic tunnel junction on top of the second interface of the ferromagnet, which enables a large readout signal.

*krishnag@mat.ethz.ch

†kurenkov@riec.tohoku.ac.jp

‡s-fukami@riec.tohoku.ac.jp

§pietro.gambardella@mat.ethz.ch

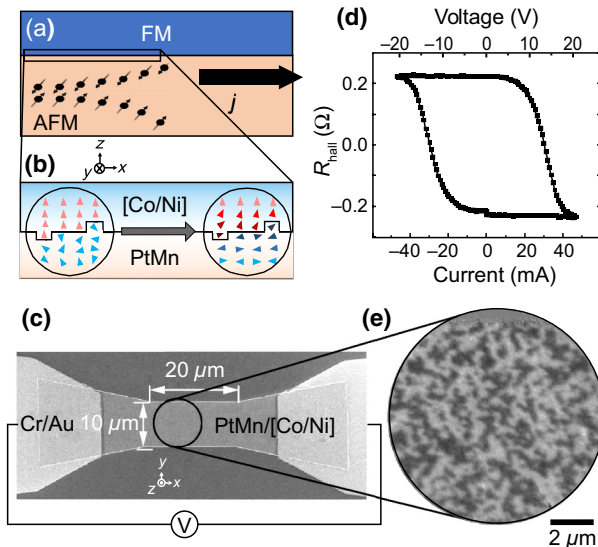


FIG. 1. (a) A schematic of an AFM/FM bilayer with current-induced spin accumulation. (b) The AFM-FM interface is magnified to show the tilt of the ferromagnetic moments induced by exchange bias, which is akin to an effective magnetic field parallel to the current. (c) A scanning electron micrograph of a patterned AFM-FM wire with Au electrodes. (d) The anomalous Hall resistance measured as a function of the applied current, showing hysteretic field-free magnetization reversal. (e) Ferromagnetic domains observed by XPEEM in PtMn(9.5)/[Co/Ni]_{2.5} after a voltage pulse of -16 V during a hysteresis cycle starting from $+20$ V. The field of view has a diameter of 10 μm . Regions with dark and bright contrast represent domains with opposite out-of-plane magnetization.

In this study, we investigate a Co/Ni multilayer with perpendicular magnetic anisotropy that is exchange coupled to Pt₃₈Mn₆₂ (henceforth referred to as PtMn). This system exhibits field-free SOT switching as well as unique analoglike memristive magnetic states [33]. The magnetization of PtMn/[Co/Ni] devices can be manipulated by SOTs and even used to produce prototype artificial neural networks and other memristor applications [33,40–43]. One proposed explanation for the memristive behavior of PtMn/[Co/Ni] multilayers relies on the inhomogeneous distribution of exchange bias among different grains of the polycrystalline antiferromagnetic layer. Variations in the magnitude and direction of the exchange-bias field in different areas of the sample promote the switching of ferromagnetic domains coupled to antiferromagnetic grains that are biased along the current direction [33,34,40]. This hypothesis suggests that the switching of antiferromagnet (AFM)–ferromagnet (FM) bilayers has a strong granular character, different from the switching of heavy metal–ferromagnet bilayers, which unfolds by the nucleation and propagation of one or a few reversed domains across the entire sample [19,20]. This explanation still requires direct experimental verification. Other questions

concern the domain morphology and the physical mechanism of magnetization reversal in these structures. The size of the ferromagnetic and antiferromagnetic domains, how they mutually affect each other, and whether domain-wall motion or grain-by-grain switching governs the reversal of the ferromagnet are still unknown. The aim of this work is to shed light on these questions using element-specific x-ray photoemission microscopy (XPEEM) imaging and to ultimately determine how the memristivity arises in order to understand the switching behavior of AFM-FM structures and optimize the performance of artificial neural networks based on these systems.

II. EXPERIMENTAL METHODS

The samples are deposited using magnetron sputtering on naturally oxidized highly resistive Si substrates [44]. The stack structure is Si/Ta(3)/Pt(2.5)/Pt₃₈Mn₆₂(9.5)/Pt(0.6)/[Co(0.3)/Ni(0.6)]₂/Co(0.3)/MgO(1)/Ru(1), where the numbers in parentheses indicate the thickness in nanometers. To study the correlation between the ferromagnetic and antiferromagnetic domains, additional samples with the structure Si/Ta(3)/Pt(2.5)/Pt₃₈Mn₆₂(8.5)/Co(0.3)/Ni(0.6)/Co(0.3)/MgO(1.2)/Ru(0.5) are fabricated. This stack has a thinner ferromagnet and capping layers in order to allow for XPEEM imaging of PtMn. The removal of the Pt(0.6 nm) and one repetition of Co/Ni reduces the magnetic anisotropy and exchange bias without significantly changing the current-induced switching. This sample behaves qualitatively similarly to the previous one while enabling us to image the AFM and FM domains in a comparative manner [33,40,44]. Henceforth, we will refer to the two types of samples as PtMn/[Co/Ni]_{2.5} and PtMn/[Co/Ni]_{1.5}, respectively. The multilayers are annealed at 300 °C at 1.2 T in order to align the antiferromagnetic spins parallel to the current line and to introduce an exchange bias. According to prior studies, the exchange-bias field is expected to be of the order of 10–20 mT [40]. Magnetometry measurements support the existence of both perpendicular magnetic anisotropy and exchange bias. Previous studies suggest that the as-grown PtMn layers have a face centered cubic polycrystalline structure, which changes to a face centered tetragonal phase with L1₀ ordering after annealing [45]. The grain-size distribution determined by transmission electron microscopy has a mean of 12 nm and standard deviation of 3 nm. Photolithography and Ar ion milling are used to pattern multiple-wire devices of dimension 20 $\mu\text{m} \times 10$ μm , as shown in Fig. 1(c). Control devices with Hall probes are patterned on the same samples to carry out electrical switching tests prior to the XPEEM experiments. The sample coordinates are defined such that \hat{z} is normal to the sample plane and \hat{x} is the current direction.

Preliminary field-free switching tests of PtMn/[Co/Ni] are performed by measuring the anomalous Hall resistance

after the injection of current pulses. One such test is shown in Fig. 1(d), where the Hall resistance is plotted as a function of the applied current to a PtMn(9.5)/[Co/Ni]_{2.5} Hall bar. The measurement consists of an initialization pulse with an amplitude of +20 V repeated 20 times, followed by a sequence of 10-ms-long voltage pulses of increasing magnitude up to -20 V and back to +20 V, all performed at zero external field. The anomalous Hall resistance, which is proportional to the out-of-plane magnetization of the ferromagnet, is recorded after each pulse [square dots in Fig. 1(d)]. This measurement shows that the perpendicular component of the magnetization changes in an analoglike manner according to the magnitude of the applied voltage, in agreement with previous studies [33,40].

Element-resolved XPEEM imaging is performed in an ultrahigh-vacuum chamber at room temperature at the L_3 absorption edge of Co (778.6 eV), Ni (852.8 eV) and Mn (640.6 eV) with the x-ray beam incident at 16° to the sample plane. The PEEM collects the secondary electrons generated in the electron cascade following the x-ray absorption process, which limits the probing depth to about 5 nm or less. X-ray magnetic circular dichroism (XMCD) is used to achieve contrast between the up and down magnetic moments of the Co/Ni multilayer. Images obtained at the L_3 edge using right and left circular light, normalized by images acquired off resonance, are subtracted in order to form an XMCD image with maximum magnetic contrast. As the Ni and Co domain patterns are found to match, only images recorded at the Co edge are presented here. The PtMn/[Co/Ni] wires are pulsed in sequences of 10 ms-long voltage pulses with an amplitude between -20 V and 20 V while imaging the ferromagnetic domains. Here, 20 V corresponds to a current density of about $3.3 \times 10^{11} \text{ A/m}^2$. A typical domain pattern imaged after applying a pulse of -16 V is shown in Fig. 1(e). X-ray magnetic linear dichroism (XMLD) at the L_3 absorption edge of Mn is used to characterize the antiferromagnetic domain structure of PtMn in the PtMn(8.5)/[Co/Ni]_{1.5} multilayer. The XMLD contrast is obtained by subtracting two XPEEM images taken with the same linear polarization at x-ray energies corresponding to the maximum and minimum of the XMLD spectrum [46], namely 640.4 eV and 641.2 eV, and normalizing the subtracted image by their sum [47]. Both linear-horizontal (LH) and linear-vertical (LV) polarization are used, which have the electric field vector parallel to the sample plane and at an angle of 16° with respect to the sample normal, respectively.

III. RESULTS AND DISCUSSION

A. Ferromagnetic domain structure

Figure 2 shows (a) an x-ray absorption image and (b) an XMCD image of a PtMn/[Co/Ni]_{1.5} Hall bar recorded at the Co L_3 edge prior to pulsing. The uniform absorption

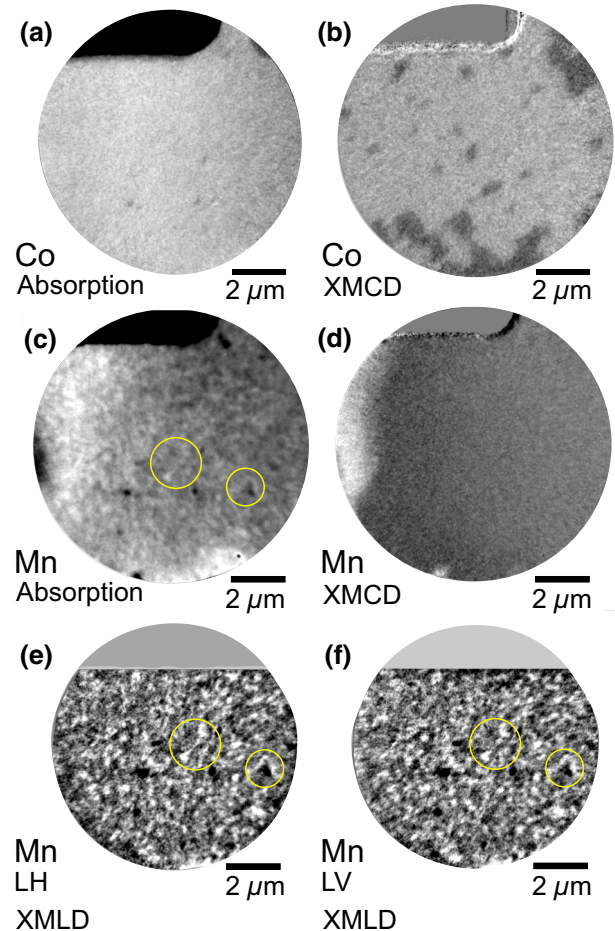


FIG. 2. XPEEM images of PtMn/[Co/Ni]_{1.5}. (a) The x-ray absorption and (b) the XMCD image at the Co L_3 edge. A corner of the Hall bar is visible on the upper side of the images. (c) The x-ray absorption and (d) the XMCD image at the Mn L_3 edge. The bright and dark regions in (c) correspond to stronger and weaker absorption, respectively. Note that uneven illumination by the x rays leads to a brighter halo on the left of the field of view, which is not related to either elemental or magnetic contrast. (e,f) The XMLD images with (e) LH and (f) LV polarization at the Mn L_3 edge. The LH-polarization axis lies parallel to the field-cooling direction of PtMn. Yellow circles highlight regions with similar contrast in (c), (e), and (f).

contrast indicates that the Co layer has a homogeneous composition and thickness. The dark and bright regions in the XMCD image represent magnetic domains with magnetization pointing toward $-\hat{z}$ and $+\hat{z}$, corresponding to positive and negative Hall resistance, respectively. We observe that the ferromagnetic domain size varies from about 200 nm to 1 μm , which is much larger than the average grain size of PtMn (approximately 15 nm) that has previously been assumed to determine the extension of the ferromagnetic domains [33,40]. Remarkably, the domain morphology bears a close resemblance in shape and size to that of Co/Ni multilayers with perpendicular

magnetic anisotropy grown on a nonmagnetic substrate [48], irrespective of the presence of PtMn.

B. Antiferromagnetic domain structure

Contrary to Co/Ni, imaging the x-ray absorption contrast at the Mn L_3 edge reveals a grainy pattern with regions of stronger and weaker absorption [Fig. 2(c)]. Such a contrast cannot be attributed to a variation of the photoelectron work function arising from surface roughness, which would otherwise also show up in images taken at the Co and Ni absorption edges. Hence, we attribute the grainy contrast in the Mn absorption to the presence of crystal grains with differently oriented crystallographic domains and/or inhomogeneous Mn concentration of the ordered PtMn structure [49–51]. The XMCD images, on the other hand, show no discernible contrast at the Mn edge within the resolution of PEEM [Fig. 2(d)], consistently with the antiferromagnetic nature of PtMn.

The antiferromagnetic domains of PtMn are investigated by taking LH and LV XMLD images as described in Sec. II, similar to previous studies performed on CuMnAs [52] and Mn₂Au [47]. The XMLD asymmetry, obtained using a single polarization, is sensitive not only to the direction of the Néel vector [53] but also to the morphological contrast originating from the subtraction of two absorption images measured on and off the L_3 edge. Indeed, the LH and LV XMLD images shown in Figs. 2(e) and 2(f), respectively, present a grainy structure that is very similar to the absorption contrast in Fig. 2(c). In order to differentiate between magnetic and nonmagnetic contrast, we record a set of XMLD images by rotating the sample about the \hat{z} axis, as shown in Fig. 3(a). Both the LH and the LV images show diffuse changes of the contrast level and/or grainy structure as a function of the incidence angle of the x rays. Given that the lattice constant of fct crystal grains in PtMn differs only by about 1% relative to the fcc phase [50], it is unlikely that such changes are due only to natural linear dichroism. Thus, the changing XMLD intensity as a function of the polarization angle might originate from antiferromagnetic domains of the PtMn layer with different orientation of the Néel vector.

Although the complexity of the PtMn structure and the spatial resolution of XPEEM do not allow us to establish a one-to-one correlation between antiferromagnetic domains and the crystalline grains of PtMn, we can draw the following preliminary conclusions from the comparison of the data presented above. The PtMn has an irregular finer grainy structure with grain orientations and/or inhomogeneous Mn concentration, which has dimensions comparable with the polycrystalline grain distribution on the scale of 10 nm, as observed in transmission electron microscopy [40]. In practice, about 34.2% of the grains are smaller than 50 nm, i.e., below or close to the

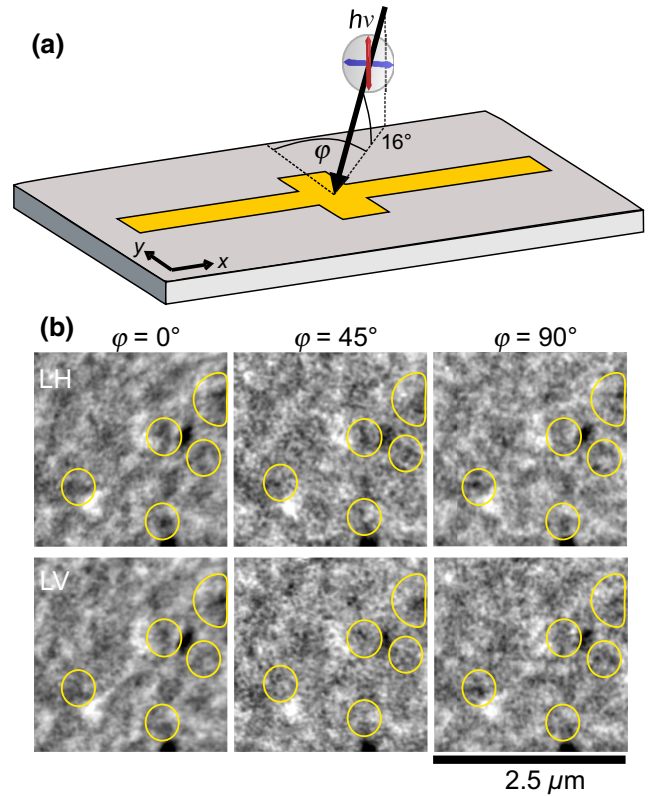


FIG. 3. The XMLD of PtMn/[Co/Ni]_{1.5} as a function of the x-ray incidence angle. (a) A schematic of the probing geometry: x rays with either LH (blue) or LV (red) polarization are incident at an angle ϕ relative to the \hat{y} direction. (b) The LH (top) and LV (bottom) images are shown at $\phi = 0^\circ$, 45° and 90° . The yellow circles highlight regions with changing contrast as a function of ϕ in both the LH and the LV images.

limit of XPEEM resolution that constitutes the finer structures. Also, 28% have dimensions between 50 and 100 nm and 24.3% between 100–200 nm. The size distribution extracted from the XMLD images in Fig. 2(c) shows that the average size of the bright (dark) regions is 165 nm (185 nm) in equivalent diameter and the number of domains decays exponentially with size, above 100 nm. The maximum size of the antiferromagnetic domains compatible with the analysis of the XMLD images at different angles of incidence is on the order of 100–200 nm, with most domains having an even smaller size. This length scale forms an upper limit for the size of the magnetic domains as they cannot be larger than the physical boundaries dictated by clusters of grains. We also infer from the XMCD-PEEM images that the ferromagnetic domains in Co/Ni are much larger than the antiferromagnetic domains in PtMn and bear no evident correlation to the underlying texture of the antiferromagnet. Finally, unlike epitaxial antiferromagnetic layers such as CuMnAs [54] and Mn₂Au [47,55], which are characterized by a biaxial domain structure, the polycrystalline PtMn layers present domains with

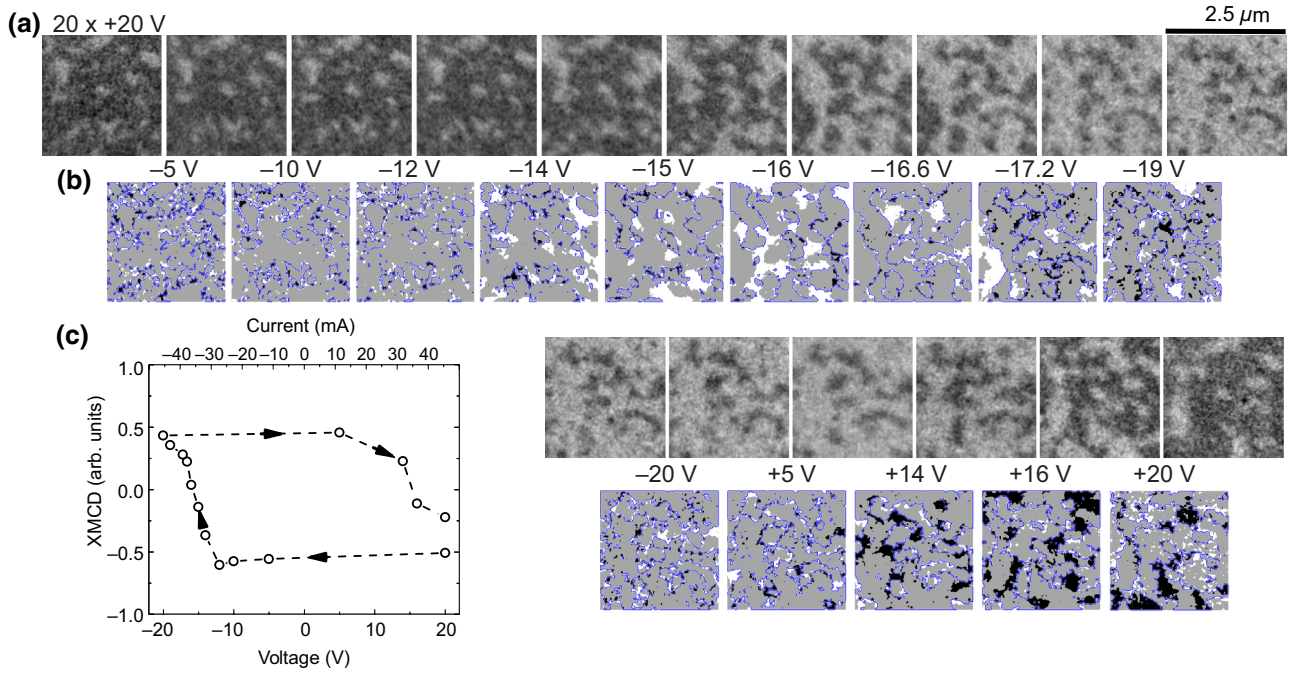


FIG. 4. The current-induced domain switching of PtMn/[Co/Ni]_{2.5}. (a) The domain structure as a function of the pulse voltage imaged by XMCD at the Co L_3 edge. The first image shows the initial state prepared by applying 20 consecutive pulses with amplitude +20 V. The amplitude of the voltage pulses is then varied in steps of 0.2 V between +20 V and -20 V before the pulse direction is reversed to return to +20 V and complete the loop. The XMCD images are taken at intermediate voltage steps, as indicated in the figure. (b) The difference between two consecutive XMCD images shown in (a). The blue lines represent the initial domain boundaries and the white (black) regions are areal increments of a bright (dark) domain. The gray regions represent areas that do not switch in between two images. The sequence depicts sequential growth of domains occurring at existing domain edges and coalescing with nearby domains of the same type. On average, only bright (dark) domains grow for negative (positive) voltage pulses. (c) The normalized magnetization obtained by integrating the XMCD contrast. The black and red dots represent measurements taken during the first and second loop, respectively; only images from the first loop are shown.

multiple orientations of the Néel vector due to variations of the local crystallographic axes and composition.

C. Current-induced memristive switching

1. Domain switching

In order to characterize the hysteretic switching mechanism of the ferromagnetic layer, we image the Co domains at a fixed position on a PtMn/[Co/Ni]_{2.5} wire during a sequence of 10 ms-long voltage pulses. The sample is first initialized by applying 20 consecutive pulses at +20 V. Following this, single pulses of decreasing amplitude are applied in steps of 0.2 V. The voltage is first decreased from +20 V to -20 V and then increased back to +20 V, thus completing a full magnetization cycle. The domain configurations recorded at intermediate voltages are shown in Fig. 4(a).

The XMCD images show that switching proceeds by the sequential reversal of domains as a function of the voltage. The initial state is mostly magnetized into dark domains; as the pulse amplitude decreases, the white domains increase in size until -20 V is reached. The application of a voltage in the opposite direction allows the dark domains to

expand again. It can be seen that the initial and final states at +20 V do not have an equal proportion of dark and bright domains. This deviation in magnetization is a consequence of the large number of initiation pulses, as several pulse repetitions switch a larger portion of the observed area compared to a single pulse [43].

To shed light on the switching mechanism, we look at the regions of domain increments between two pulses. These are depicted in Fig. 4(b), where the blue lines represent the domain boundaries before the next pulse, the white regions indicate growth of the bright domains, and the black regions indicate growth of the dark domains. Significant growth of the bright domains starts at pulse amplitudes between -12 V and -14 V. This shows that the threshold voltage is around -12 V (estimated current density approximately $1.8 \times 10^{11} \text{ A/m}^2$). The expansion of only one domain type during pulsing, which depends on the sign of the voltage, confirms that switching is due to SOT rather than Joule heating. Interestingly, domain growth mainly occurs at the edges of existing domains, whereas few nucleation of new domains is observed. This is unexpected because if the switching was merely grain by grain, many independent nucleation sites would emerge as

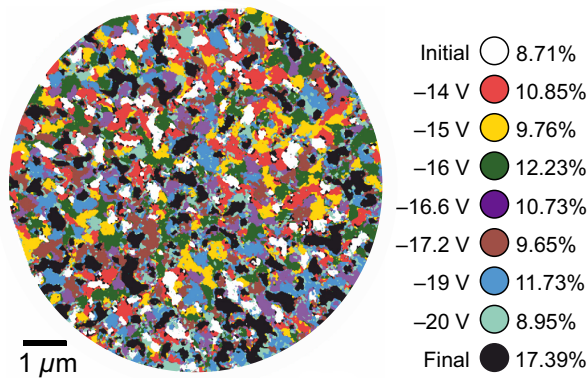


FIG. 5. A color map of the incremental domain switching in PtMn/[Co/Ni]_{2.5}. The initial and final minority domains are represented in white and black, respectively. Subsequent areal increments are shown, starting from -14 V down to -20 V. Each color represents the increase in domain size after a single pulse.

a function of voltage. The edge-mediated domain increments suggest that switching may occur via domain-wall motion. However, we observe no definite directionality of the domain increments compared to the current direction, which would be expected for SOT-induced propagation of chiral domain walls [20,56,57]. The lack of directionality in this case may be due to the presence of achiral domain walls in PtMn/[Co/Ni] or to the highly inhomogeneous domain-pinning landscape provided by the exchange-bias variation due to the polycrystalline PtMn layer. Additionally, the high density of domains, as well as the tendency of nearby domains to coalesce, make it difficult to identify directional motion of domain walls.

The domain-switching sequence shown in Fig. 4(a) reproduces well the analog switching behavior of AFM/FM bilayers evidenced in previous work [33,40]. This can be seen by plotting the normalized intensity of each XMCD image as a function of the voltage, which is directly proportional to the perpendicular component of the magnetization. Figure 4(c) shows that the normalized XMCD intensity follows a hysteretic curve comparable to the anomalous Hall resistance reported in Fig. 1(d). Further evidence for the analog switching behavior is presented in Fig. 5, where we map the fraction of domains that switch at a given voltage. Each color represents an increase in the domain size after a voltage pulse, which shows that the pulses tend to switch nearby granular regions in a sequential way.

2. Blocked domains

Despite repetitive pulsing, complete saturation of the magnetization cannot be achieved at either $+20$ V or -20 V, the maximum voltage utilized in this study. We compare two domain states in Fig. 6, one at $+20$ V (a) and another at -20 V (b), reached after applying single pulses

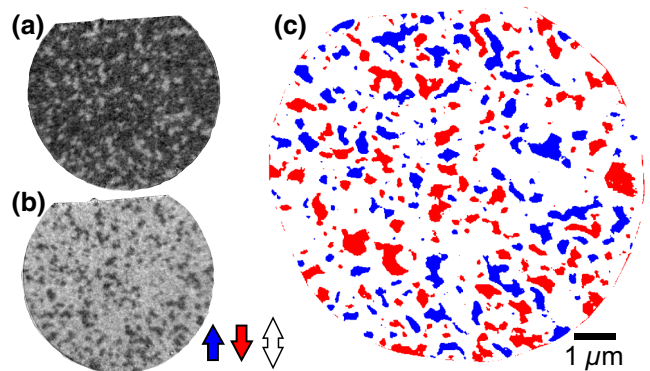


FIG. 6. Images of PtMn/[Co/Ni]_{2.5} taken after a pulse of (a) $+20$ V and (b) -20 V during a hysteresis loop show two incomplete saturation states with minority blocked domains. (c) The regions of perennial bright and dark contrast obtained from averaging all images in the hysteresis loop show the spatial distribution of the blocked domains: blue (red) corresponds to bright (dark) domains in the up (down) states, with the magnetization oriented along the sample normal.

in incremental steps of 0.2 V during a hysteresis loop. Remarkably, we observe that at $+20$ V (dark state) approximately 22% of the image area is occupied by minority bright domains and at -20 V (bright state) approximately 24% of the image area is occupied by minority dark domains. To confirm whether these are truly blocked, we average XMCD images taken over three hysteresis cycles. On averaging all the images in three hysteresis loops, we can identify regions that are always bright and dark and these are shown in Fig. 6(c). We find bright domains occupying $11 \pm 7\%$ and dark domains occupying $13 \pm 7\%$, together adding up to $24 \pm 13\%$ of the area that is always blocked and cannot switch. While the positions of these regions shown in Fig. 6(c) correlate quite well with the minority domains observed in the two saturated states in Figs. 6(a) and 6(b), the percentages are much lower and there are variations in the shape. This difference in percentage suggests that some of the minority regions observed in Figs. 6(a) and 6(b) switch in a nondeterministic manner.

The bright and dark minority domains that are blocked occupy different areas of the sample, as shown in Fig. 6(c). The positions of the blocked domains are likely determined by the inhomogeneous exchange-bias distribution of the granular PtMn layer. Regions with a very large out-of-plane component of the exchange bias could pin the ferromagnetic domains too steadily for switching to occur. Alternatively, regions with weak in-plane exchange bias along the current direction could not provide an effective field that is strong enough to allow for deterministic SOT switching, leading to the stochastic reversal of the weakly exchange-biased regions. Incomplete saturation appears to be a general feature of PtMn/[Co/Ni] multilayers. Prior studies have shown that, while it is possible to saturate the

anomalous Hall resistance of PtMn/[Co/Ni] devices under an external field, the anomalous Hall signal decreases upon removal of the field [33]. Such behavior can be attributed to the presence of minority domains that switch back upon removal of the external magnetic field, which further suggests that these domains are strongly pinned by exchange bias rather than being weakly pinned.

The blocked domains play an important role in the switching mechanism of the Co/Ni layer as well as in the reproducibility of the switching path. The blocked domains act as the starting points for domain growth when the threshold current is reached. Figure 6(c) shows how densely packed and dispersed in size the blocked regions are. On inspecting sequences of consecutive XMCD images, we observe that reversed domains expand across regions that are free to switch, often connecting the closest blocked domains of the same species. Thus, the regions between two blocked domains tend to reverse before the surrounding areas. We conclude that the switching of the Co/Ni layer proceeds by expansion of the blocked domains and is constrained by the network of the blocked areas, which determines the expansion path of the free domains. The latter has a strong influence on the reproducibility of the switching process, as discussed in the next section.

3. Reproducible switching patterns

We further focus on some aspects of the switching that are important in explaining the memristive behavior of AFM/FM bilayers. In conventional ferromagnets, it is generally possible to achieve the same net magnetization with different domain configurations. This, however, might not lead to reproducible intermediate states. Conversely, if the same domain structure is reproduced at each step, the same magnetization can be achieved. If the domain structure depends in a reproducible way on the device history, the magnetization has a memory of the applied electrical pulses, which is a necessary condition to realize a magnetic memristor. To check this, we compare images recorded at the same voltage during successive switching cycles of PtMn/[Co/Ni]_{2.5}. If the switching was to occur at random, reproducible intermediate states would not be possible. In Figs. 7(a) and 7(b), two enlarged areas of the images taken at -15 V during the second and third hysteresis loops, respectively, are shown. We observe that the bright and dark domains do not overlap exactly but roughly occupy the same position and have a similar shape between the two images, which is remarkable since each voltage loop corresponds to a sequence of 400 pulses in increments of 0.2 V. The agreement in domain areas between the first and second cycles (not shown) is lower than that between the second and third cycles, as the initial states are different due to the larger number of pulse repetitions at +20 V used to initialize the magnetization before the first cycle. This

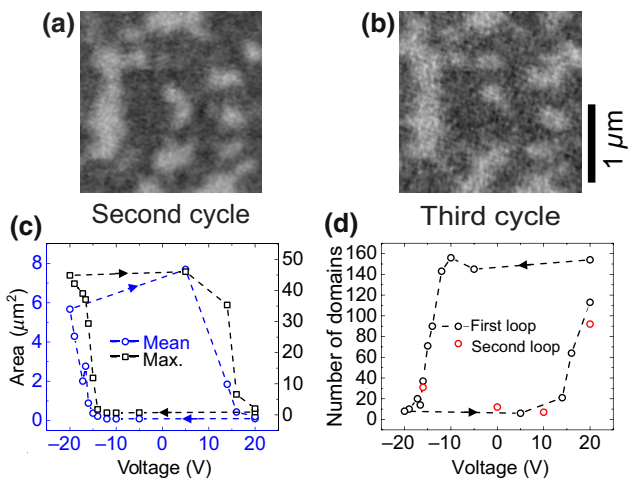


FIG. 7. Reproducible domain switching in PtMn/[Co/Ni]_{2.5}. A comparison between two XMCD images of the same area recorded after pulsing at -15 V starting from +20 V during the (a) second and (b) third switching cycle. (c) The calculated domain areas as a function of the voltage. The circles and squares represent the mean and maximum area, respectively, of the bright domains. (d) The number of bright domains as a function of the voltage. The black and red symbols in (d) represent data acquired during the first and second switching cycle, respectively, obtained after digitizing the magnetic contrast in each image.

shows that the reproducibility can be trained with multiple cycles. Integrating the magnetic contrast over large area images further shows that the small differences in the switching domain areas cancel out, resulting in an even higher degree of reproducibility for the macroscopic magnetization [Fig. 4(c)].

Additional metrics of reproducibility can be obtained by performing real-space edge detection of domains, which allows for calculation of the domain area and counting of the domains in each image of the hysteresis loop. Figure 7(c) shows the mean (circle symbols) and maximum area (square symbols) of the bright domains during the first and second hysteresis cycles. Starting from a single percolated dark domain and a dispersed distribution of small bright domains at +20 V, the mean area of the bright domains starts to increase at about -15 V, reaches a maximum at -20 V, and decreases again upon returning to +20 V. The area of the largest bright domain follows a similar behavior but expands at a faster rate compared to the mean area owing to the coalescent behavior discussed in Sec. 2. The number of domains, plotted in Fig. 7(d), is also hysteretic. Starting from many small bright domains at +20 V, we observe the first significant change in number at about -12 V, consistently with the observations reported in Sec. 1. The decrease in domain number occurring for pulses of larger negative amplitude indicates that no new domains are created beyond the threshold

switching voltage, in agreement with the proposed mechanism of domain expansion and coalescence starting from a pre-existing population of blocked domains. The reproducibility in both the area and the number of domains further supports our conclusion that coalescence must happen along specific paths defined by the network of blocked domains of the opposite species, which is crucial for the observed reproducible switching and memristive behavior of PtMn/[Co/Ni] multilayers.

IV. CONCLUSION

In summary, we study the structure and current-induced switching behavior of the magnetic domains in PtMn/[Co/Ni]_{1.5} and PtMn/[Co/Ni]_{2.5} multilayers. Element-resolved XPEEM images show that the Co/Ni layers have a homogenous composition and thickness, whereas PtMn presents a granular structure attributed to the inhomogeneous orientation and/or composition of the PtMn crystal grains. The size of the PtMn grains evidenced by XPEEM ranges from about 200 nm to below the instrumental resolution of about 50 nm, which is compatible with the upper range of the grain distribution measured by transmission electron microscopy [40]. XMLD images recorded with either LH or LV polarization indicate that the antiferromagnetic domains have a size comparable or smaller than the granular structure of PtMn. The ferromagnetic domains in Co/Ni are generally much larger than the antiferromagnetic domains, up to several micrometers wide, and do not show a strict correlation with the underlying texture of PtMn. However, the presence of blocked ferromagnetic domains as well as the reproducibility of the switching behavior indicate that local pinning of the ferromagnet by one or more PtMn grains plays a dominant role in the current-induced switching process.

XMCD imaging as a function of the electrical pulses shows that switching of Co/Ni occurs by domain expansion driven by SOT and proceeds incrementally upon repeated pulsing beyond a current threshold of about $1.8 \times 10^{11} \text{ A/m}^2$. Switching starts from the edges of blocked domains and proceeds by domain-wall displacement rather than grain by grain. No significant nucleation of new domains is observed during pulsing, whereas the blocked domains expand and eventually coalesce, creating a single percolated domain. Due to the presence of the blocked domains, the maximum saturation level reached upon multiple pulsing at a current density of about $3.3 \times 10^{11} \text{ A/m}^2$ is about 75%.

The domain pattern is found to be highly reproducible between consecutive switching cycles, both in terms of the position and the number of domains. This reproducibility is partly attributed to the presence of the blocked domains, which provide a stable network of starting points for domain expansion and constrain the motion of the domain walls between them. The distribution of exchange

bias due to different PtMn grains or clusters of grains and their interplay with the symmetry of SOTs is also likely to influence the domain-wall motion, as suggested in previous studies [33,34,40]. Together, the stepwise expansion of the domains starting from blocked domains and the reproducibility of the domain pattern determine the memristive properties of this system. Future studies may address the influence of the thickness of the antiferromagnet, perpendicular magnetic anisotropy, and the distribution of the in-plane and out-of-plane exchange bias on the switching dynamics and memristive behavior of AFM-FM structures.

ACKNOWLEDGMENTS

This work was supported by the Swiss National Science Foundation (Grant No. 200020-172775), the “Impulsing PAradigm Change through disruptive Technologies” (ImPACT) Program of the Council for Science, Technology, and Innovation (CSTI), the Japan Society for the Promotion of Science (JSPS) Grants-in-Aid for Scientific Research (KAKENHI) Grants No. 18KK0143 and No. 19H05622, the Japan Science and Technology Agency (JST) Core Research for Evolutional Science and Technology (CREST) Grant No. JPMJCR19K3, the JSPS Core-to-Core Program, Cooperative Research Projects of the Research Institute of Electrical Communication (RIEC), and the Convenient Access to Light Sources Open to Innovation, Science, and to the World (CALIPSOplus) project of Horizon 2020, the EU Framework Programme for Research and Innovation (Grant Agreement No. 730872). V.K. acknowledges partial support from a Swiss Government Excellence Scholarship (ESKAS-Nr. 2018.0056).

- [1] A. Manchon, J. Železný, I. M. Miron, T. Jungwirth, J. Sinova, A. Thiaville, K. Garello, and P. Gambardella, Current-induced spin-orbit torques in ferromagnetic and antiferromagnetic systems, *Rev. Mod. Phys.* **91**, 035004 (2019).
- [2] I. M. Miron, K. Garello, G. Gaudin, P. J. Zermatten, M. V. Costache, S. Auffret, S. Bandiera, B. Rodmacq, A. Schuhl, and P. Gambardella, Perpendicular switching of a single ferromagnetic layer induced by in-plane current injection, *Nature* **476**, 189 (2011).
- [3] C. O. Avci, K. Garello, I. Mihai Miron, G. Gaudin, S. Aufret, O. Boulle, and P. Gambardella, Magnetization switching of an MgO/Co/Pt layer by in-plane current injection, *Appl. Phys. Lett.* **100**, 212404 (2012).
- [4] L. Liu, C.-F. Pai, Y. Li, H. W. Tseng, D. C. Ralph, and R. A. Buhrman, Spin-torque switching with the giant spin Hall effect of tantalum, *Science* **336**, 555 (2012).
- [5] C.-F. Pai, L. Liu, Y. Li, H. W. Tseng, D. C. Ralph, and R. A. Buhrman, Spin transfer torque devices utilizing the giant spin Hall effect of tungsten, *Appl. Phys. Lett.* **101**, 122404 (2012).

- [6] W. Zhang, M. B. Jungfleisch, W. Jiang, J. E. Pearson, and A. Hoffmann, Spin pumping and inverse Rashba-Edelstein effect in NiFe/Ag/Bi and NiFe/Ag/Sb, *J. Appl. Phys.* **117**, 17C727 (2015).
- [7] M. Akyol, W. Jiang, G. Yu, Y. Fan, M. Gunes, A. Ekicibil, P. Khalili Amiri, and K. L. Wang, Effect of heavy metal layer thickness on spin-orbit torque and current-induced switching in Hf/CoFeB/MgO structures, *Appl. Phys. Lett.* **109**, 022403 (2016).
- [8] S. Fukami, T. Anekawa, C. Zhang, and H. Ohno, A spin-orbit torque switching scheme with collinear magnetic easy axis and current configuration, *Nat. Nanotechnol.* **11**, 621 (2016).
- [9] R. Ramaswamy, X. Qiu, T. Dutta, S. D. Pollard, and H. Yang, Hf thickness dependence of spin-orbit torques in Hf/CoFeB/MgO heterostructures, *Appl. Phys. Lett.* **108**, 202406 (2016).
- [10] A. Ghosh, K. Garello, C. O. Avci, M. Gabureac, and P. Gambardella, Interface-Enhanced Spin-Orbit Torques and Current-Induced Magnetization Switching of Pd/Co/AlO_x Layers, *Phys. Rev. Appl.* **7**, 014004 (2017).
- [11] K. Garello, I. M. Miron, C. O. Avci, F. Freimuth, Y. Mokrousov, S. Blügel, S. Auffret, O. Boulle, G. Gaudin, and P. Gambardella, Symmetry and magnitude of spin-orbit torques in ferromagnetic heterostructures, *Nat. Nanotechnol.* **8**, 587 (2013).
- [12] J. Kim, J. Sinha, M. Hayashi, M. Yamanouchi, S. Fukami, T. Suzuki, S. Mitani, and H. Ohno, Layer thickness dependence of the current-induced effective field vector in Ta/CoFeB/MgO, *Nat. Mater.* **12**, 240 (2013).
- [13] P. M. Haney, H.-W. Lee, K.-J. Lee, A. Manchon, and M. Stiles, Current induced torques and interfacial spin-orbit coupling: Semiclassical modeling, *Phys. Rev. B* **87**, 174411 (2013).
- [14] V. P. Amin, J. Zemen, and M. D. Stiles, Interface-Generated Spin Currents, *Phys. Rev. Lett.* **121**, 136805 (2018).
- [15] C. O. Avci, G. S. D. Beach, and P. Gambardella, Effects of transition metal spacers on spin-orbit torques, spin Hall magnetoresistance, and magnetic anisotropy of Pt/Co bilayers, *Phys. Rev. B* **100**, 235454 (2019).
- [16] I. M. Miron, G. Gaudin, S. Auffret, B. Rodmacq, A. Schuhl, S. Pizzini, J. Vogel, and P. Gambardella, Current-driven spin torque induced by the Rashba effect in a ferromagnetic metal layer, *Nat. Mater.* **9**, 230 (2010).
- [17] I. M. Miron, T. Moore, H. Szambolics, L. D. Buda-Prejbeanu, S. Auffret, B. Rodmacq, S. Pizzini, J. Vogel, M. Bonfim, A. Schuhl, and G. Gaudin, Fast current-induced domain-wall motion controlled by the Rashba effect, *Nat. Mater.* **10**, 419 (2011).
- [18] S. Emori, U. Bauer, S.-M. Ahn, E. Martinez, and G. S. D. Beach, Current-driven dynamics of chiral ferromagnetic domain walls, *Nat. Mater.* **12**, 611 (2013).
- [19] G. Yu, P. Upadhyaya, K. L. Wong, W. Jiang, J. G. Alzate, J. Tang, P. K. Amiri, and K. L. Wang, Magnetization switching through spin-Hall-effect-induced chiral domain wall propagation, *Phys. Rev. B* **89**, 104421 (2014).
- [20] M. Baumgartner, K. Garello, J. Mendil, C. O. Avci, E. Grimaldi, C. Murer, J. Feng, M. Gabureac, C. Stamm, Y. Acremann, S. Finizio, S. Wintz, J. Raabe, and P. Gambardella, Spatially and time-resolved magnetization dynamics driven by spin-orbit torques, *Nat. Nanotechnol.* **12**, 980 (2017).
- [21] S.-W. Lee and K.-J. Lee, Emerging three-terminal magnetic memory devices, *Proc. IEEE* **104**, 1831 (2016).
- [22] S. Fukami and H. Ohno, Magnetization switching schemes for nanoscale three-terminal spintronics devices, *Jpn. J. Appl. Phys.* **56**, 0802A1 (2017).
- [23] K. Garello, C. O. Avci, I. M. Miron, M. Baumgartner, A. Ghosh, S. Auffret, O. Boulle, G. Gaudin, and P. Gambardella, Ultrafast magnetization switching by spin-orbit torques, *Appl. Phys. Lett.* **105**, 212402 (2014).
- [24] M. Cubukcu, O. Boulle, M. Drouard, K. Garello, C. Onur Avci, I. Mihai Miron, J. Langer, B. Ocker, P. Gambardella, and G. Gaudin, Spin-orbit torque magnetization switching of a three-terminal perpendicular magnetic tunnel junction, *Appl. Phys. Lett.* **104**, 042406 (2014).
- [25] A. van den Brink, S. Cosemans, S. Cornelissen, M. Manfrini, A. Vaysset, W. Van Roy, T. Min, H. J. M. Swagten, and B. Koopmans, Spin-Hall-assisted magnetic random access memory, *Appl. Phys. Lett.* **104**, 012403 (2014).
- [26] M. Cubukcu, O. Boulle, N. Mikuszeit, C. Hamelin, T. Brächer, N. Lamard, M.-C. Cyrille, L. Buda-Prejbeanu, K. Garello, I. M. Miron, O. Klein, G. de Loubens, V. V. Naletov, J. Langer, B. Ocker, P. Gambardella, and G. Gaudin, Ultra-fast perpendicular spin orbit torque MRAM, *IEEE Trans. Magn.* **54**, 9300204 (2015).
- [27] E. Grimaldi, V. Krizakova, G. Sala, F. Yasin, S. Couet, G. S. Kar, K. Garello, and P. Gambardella, Single-shot dynamics of spin-orbit torque and spin transfer torque switching in three-terminal magnetic tunnel junctions, *Nat. Nanotechnol.* **15**, 111 (2020).
- [28] K. Garello, F. Yasin, H. Hody, S. Couet, L. Souriau, S. H. Sharifi, J. Swerts, R. Carpenter, S. Rao, W. Kim, J. Wu, K. K. V. Sethu, M. Pak, N. Jossart, D. Crotti, A. Furnmont, and G. S. Kar, in *2019 Symposium on VLSI Circuits* (Kyoto, Japan, 2019), p. T194.
- [29] G. Yu, L.-T. Chang, M. Akyol, P. Upadhyaya, C. He, X. Li, K. L. Wong, P. K. Amiri, and K. L. Wang, Current-driven perpendicular magnetization switching in Ta/CoFeB/[TaO_x or MgO/TaO_x] films with lateral structural asymmetry, *Appl. Phys. Lett.* **105**, 102411 (2014).
- [30] C. K. Safeer, E. Jué, A. Lopez, L. Buda-Prejbeanu, S. Auffret, S. Pizzini, O. Boulle, I. M. Miron, and G. Gaudin, Spin-orbit torque magnetization switching controlled by geometry, *Nat. Nanotechnol.* **11**, 143 (2016).
- [31] L. You, O. Lee, D. Bhowmik, D. Labanowski, J. Hong, J. Bokor, and S. Salahuddin, Switching of perpendicularly polarized nanomagnets with spin orbit torque without an external magnetic field by engineering a tilted anisotropy, *Proc. Natl. Acad. Sci.* **112**, 10310 (2015).
- [32] Y.-C. Lau, D. Betto, K. Rode, J. M. D. Coey, and P. Stamenov, Spin-orbit torque switching without an external field using interlayer exchange coupling, *Nat. Nanotechnol.* **11**, 758 (2016).
- [33] S. Fukami, C. Zhang, S. DuttaGupta, A. Kurenkov, and H. Ohno, Magnetization switching by spin-orbit torque in an antiferromagnet/ferromagnet bilayer system, *Nat. Mater.* **15**, 535 (2016).
- [34] A. van den Brink, G. Vermijs, A. Solignac, J. Koo, J. T. Kohlhepp, H. J. M. Swagten, and B. Koopmans, Field-free

- magnetization reversal by spin-Hall effect and exchange bias, *Nat. Commun.* **7**, 10854 (2016).
- [35] Y.-W. Oh, S.-H. Chris Baek, Y. M. Kim, H. Y. Lee, K.-D. Lee, C.-G. Yang, E.-S. Park, K.-S. Lee, K.-W. Kim, G. Go, J.-R. Jeong, B.-C. Min, H.-W. Lee, K.-J. Lee, and B.-G. Park, Field-free switching of perpendicular magnetization through spin-orbit torque in antiferromagnet/ferromagnet/oxide structures, *Nat. Nanotechnol.* **11**, 878 (2016).
- [36] V. Tshitoyan, C. Ciccarelli, A. P. Mihai, M. Ali, A. C. Irvine, T. A. Moore, T. Jungwirth, and A. J. Ferguson, Electrical manipulation of ferromagnetic NiFe by antiferromagnetic IrMn, *Phys. Rev. B* **92**, 214406 (2015).
- [37] W. Zhang, M. B. Jungfleisch, W. Jiang, J. E. Pearson, A. Hoffmann, F. Freimuth, and Y. Mokrousov, Spin Hall Effects in Metallic Antiferromagnets, *Phys. Rev. Lett.* **113**, 196602 (2014).
- [38] W. Zhang, M. B. Jungfleisch, F. Freimuth, W. Jiang, J. Sklenar, J. E. Pearson, J. B. Ketterson, Y. Mokrousov, and A. Hoffmann, All-electrical manipulation of magnetization dynamics in a ferromagnet by antiferromagnets with anisotropic spin Hall effects, *Phys. Rev. B* **92**, 144405 (2015).
- [39] Y. Ou, S. Shi, D. C. Ralph, and R. A. Buhrman, Strong spin Hall effect in the antiferromagnet PtMn, *Phys. Rev. B* **93**, 220405(R) (2016).
- [40] A. Kurenkov, C. Zhang, S. DuttaGupta, S. Fukami, and H. Ohno, Device-size dependence of field-free spin-orbit torque induced magnetization switching in antiferromagnet/ferromagnet structures, *Appl. Phys. Lett.* **110**, 092410 (2017).
- [41] W. A. Borders, H. Akima, S. Fukami, S. Moriya, S. Kurihara, Y. Horio, S. Sato, and H. Ohno, Analogue spin-orbit-torque device for artificial-neural-network-based associative memory operation, *Appl. Phys. Express* **10**, 013007 (2016).
- [42] W. A. Borders, S. Fukami, and H. Ohno, Characterization of spin-orbit torque-controlled synapse device for artificial neural network applications, *Jpn. J. Appl. Phys.* **57**, 1002B2 (2018).
- [43] A. Kurenkov, S. DuttaGupta, C. Zhang, S. Fukami, Y. Horio, and H. Ohno, Artificial neuron and synapse realized in an antiferromagnet/ferromagnet heterostructure using dynamics of spin-orbit torque switching, *Adv. Mater.* **31**, 1900636 (2019).
- [44] W. A. Borders, S. Fukami, and H. Ohno, Stack structure dependence of magnetic properties of PtMn/[Co/Ni] films for spin-orbit torque switching device, *IEEE Trans. Magn.* **53**, 1 (2017).
- [45] C. X. Ji, P. F. Ladwig, R. D. Ott, Y. Yang, J. J. Yang, Y. A. Chang, E. S. Linville, J. Gao, and B. B. Pant, An investigation of phase transformation behavior in sputter-deposited PtMn thin films, *JOM* **58**, 50 (2006).
- [46] J. Fujii, F. Borgatti, G. Panaccione, M. Hochstrasser, F. Maccherozzi, G. Rossi, and G. van der Laan, Evidence for in-plane spin-flop orientation at the MnPt/Fe(100) interface revealed by x-ray magnetic linear dichroism, *Phys. Rev. B* **73**, 214444 (2006).
- [47] S. Y. Bodnar, M. Filianina, S. P. Bommanaboyena, T. Forrest, F. Maccherozzi, A. A. Sapozhnik, Y. Skourski, M. Kläui, and M. Jourdan, Imaging of current induced Néel vector switching in antiferromagnetic mn_2Au , *Phys. Rev. B* **99**, 140409(R) (2019).
- [48] M. Suzuki, K. Kudo, K. Kojima, T. Yasue, N. Akutsu, W. A. Diño, H. Kasai, E. Bauer, and T. Koshikawa, Magnetic domain patterns on strong perpendicular magnetization of Co/Ni multilayers as spintronics materials: I. dynamic observations, *J. Phys.: Condens. Matter* **25**, 406001 (2013).
- [49] A. F. Andresen, A. Kjekshus, R. Møllerud, and W. B. Pearson, Equiatomic transition metal alloys of manganese IV. A neutron diffraction study of magnetic ordering in the PtMn phase, *Philos. Mag.: J. Theor. Exp. Appl. Phys.* **11**, 1245 (1965).
- [50] A. Maesaka, S. Ishii, and A. Okabe, Transmission electron microscopy analysis of crystallographic transition from fcc to fct on PtMn spin valves, *J. Appl. Phys.* **88**, 3982 (2000).
- [51] D. E. Laughlin, K. Srinivasan, M. Tanase, and L. Wang, Crystallographic aspects of 110 magnetic materials, *Scr. Mater.* **53**, 383 (2005).
- [52] P. Wadley *et al.*, Electrical switching of an antiferromagnet, *Science* **351**, 587 (2016).
- [53] J. Stöhr and H. C. Siegmann, *Magnetism: From Fundamentals to Nanoscale Dynamics* (Springer, Berlin, 2006), Vol. 152.
- [54] P. Wadley, S. Reimers, M. J. Grzybowski, C. Andrews, M. Wang, J. S. Chauhan, B. L. Gallagher, R. P. Campion, K. W. Edmonds, S. S. Dhesi, *et al.*, Current polarity-dependent manipulation of antiferromagnetic domains, *Nat. Nanotechnol.* **13**, 362 (2018).
- [55] A. A. Sapozhnik, R. Abrudan, Y. Skourski, M. Jourdan, H. Zabel, M. Kläui, and H.-J. Elmers, Manipulation of antiferromagnetic domain distribution in mn_2au by ultrahigh magnetic fields and by strain, *Phys. Status Solidi (RRL)—Rapid Res. Lett.* **11**, 1600438 (2017).
- [56] A. Thiaville, S. Rohart, É. Jué, V. Cros, and A. Fert, Dynamics of Dzyaloshinskii domain walls in ultrathin magnetic films, *Europhys. Lett.* **100**, 57002 (2012).
- [57] M. Baumgartner and P. Gambardella, Asymmetric velocity and tilt angle of domain walls induced by spin-orbit torques, *Appl. Phys. Lett.* **113**, 242402 (2019).